Polymer 68 (2015) 158–167

Contents lists available at ScienceDirect

Polymer

journal homepage: www.elsevier.com/locate/polymer

Interfacial phenomena in core–shell nanocomposites of PDMS adsorbed onto low specific surface area fumed silica nanooxides: Effects of surface modification

P. Klonos [a, *], I.Ya. Sulym [b], K. Kyriakos [a], I. Vangelidis [a], S. Zidropoulos [a], D. Sternik [c], M.V. Borysenko [b], A. Kyritsis [a], A. Deryło-Marczewska [c], V.M. Gun'ko [b], P. Pissis [a]

[a] Department of Physics, National Technical University of Athens, Zografou Campus, 15780 Athens, Greece
[b] Chuiko Institute of Surface Chemistry, National Academy of Sciences of Ukraine, 17 General Naumov Street, Kiev 03164, Ukraine
[c] Faculty of Chemistry, Maria Curie–Skłodowska University, pl. Maria Curie–Skłodowskiej 3, 20–031 Lublin, Poland

ARTICLE INFO

Article history:
Received 27 December 2014
Received in revised form
7 May 2015
Accepted 11 May 2015
Available online 18 May 2015

Keywords:
Silica polydimethylsiloxane composite
Core–shell particles
Interfacial dynamics

ABSTRACT

Core–shell structured nanocomposites of polydimethylsiloxane (PDMS) adsorbed onto low specific surface area fumed silica nanoparticles were studied employing structure (nitrogen adsorption –desorption, IPSD), morphology (SEM), thermal (DSC) and dielectric (BDS) techniques. The study focuses on the effects of porosity characteristics on polymer structure and dynamics at the filler interface. To that aim, roughness and porosity characteristics of silica were modified, prior to polymer adsorption, with nanozirconia grafting. The initial particles (15–150 nm in diameter) were found to aggregate and disperse well in the volume of nanocomposites, while nanozirconia grafting resulted in increased volume of the voids. PDMS was adsorbed both in the inner space of the voids and onto external surfaces of the aggregates. According to BDS and DSC the fraction of polymer chains at interfaces increases with nanozirconia modification and the respective dynamics (α_{int} relaxation) and cooperativity are enhanced. The results were interpreted in terms of increasing of the number of polymer–particle contact points on the modified surfaces, as compared to the unmodified ones. Finally, the characteristics of interfacial polymer (fraction, dynamics, polarizability) were interpreted employing models which involve bimodal chain conformations and increased order (orientation) of the polymer chains at the interfaces.

1. Introduction

Polymer nanocomposites (PNCs) have attracted much interest over the last 2–3 decades for improving material properties [1]. Historically, the initial effort was on the improvement of specific properties (e.g. mechanical, thermal and chemical stability) of a polymer matrix in PNCs by introducing and well dispersing inorganic nanoparticles [1,2]. Such materials may be considered as *conventional* PNCs. Improvement of properties in PNCs is widely thought to arise from the large surface to volume ratio of nanofillers, so that a great fraction of polymer is located at interfaces with nanoparticles (the so called 'interfacial polymer fraction') [3–5]. It is now commonly accepted that the interfacial polymer fraction [4,6] is characterized by modified structure [7,8], slower dynamics [9–12], and increased thermal stability [13], as compared to the bulk. *Core–shell* nanocomposites (NCs) is a new class of NCs [14] prepared by *layer–by–layer* [15] polymer adsorption (*shells*) onto the surface of nanoparticles (*cores*) [16,17]. Next to mostly biomedical applications [18], these systems offer the possibility for an in–depth study of interfacial interactions and polymer conformations in the interfacial layer [19]: by controlling the fraction of adsorbed polymer, the interfacial polymer fraction may become the main polymer fraction in the system and, thus, more easily accessible to measurements.

Measurements in PNCs with silica [9] and titania [10] particles *in situ* generated by sol–gel techniques in the presence of polydimethylsiloxane (PDMS), the polymer of interest in the present work, revealed the existence of an interfacial polymer fraction that is characterized by reduced mobility [10] in the case of titania as compared to silica. This has been explained in terms of stronger hydrogen bonds between PDMS and titania rather than silica (Ti–OH more acidic than Si–OH) [20]. The dimensions of primary

* Corresponding author. Tel.: +30 2107722974; fax: +30 2107722932.
E-mail address: pklonos@central.ntua.gr (P. Klonos).

http://dx.doi.org/10.1016/j.polymer.2015.05.017
0032-3861/

particles affecting the surface curvature have also been considered significant for interfacial interactions [21]. More recently, measurements in core–shell NCs based on high specific surface area (~350 m^2/g, high roughness) silica revealed that the structure of the adsorption complexes of PDMS depends on the adsorption conditions and the subsequent thermal treatment [19], similarly to polymer adsorption on flat solid surfaces [6,22–24].

The present work focuses on the effects of surface and structure properties of silica nanoparticles (in the form of aggregates) on the characteristics of interfacial polymer in NCs of the *core–shell* type, based on low specific surface area (~58 m^2/g) fumed silica (~15–100 nm in size for primary particles) and physically adsorbed linear PDMS. Before polymer adsorption, the initial silica particle surfaces were partly modified by the chemical development of amorphous zirconia nanoparticles. The porosity properties of initial and modified silica and silica/PDMS NCs were investigated using low temperature nitrogen adsorption/desorption and Incremental Pore Size Distribution (IPSD) analysis. The morphology was examined employing scanning electron microscopy (SEM), while phase transitions of PDMS in the NCs were studied using differential scanning calorimetry (DSC). Finally, PDMS segmental dynamics (dynamic glass transition) at interfaces and in bulk was studied in detail using broadband dielectric relaxation spectroscopy (BDS). Results are critically discussed and compared with similar results obtained with other *core–shell* and *conventional* PDMS–based NCs.

2. Experimental

2.1. Materials and code names

Fumed silica OX–50 (Degussa, ~15–100 nm in diameter, amorphous) was used as substrate, neat and modified with zirconia. Zirconium acetylacetonate (Aldrich, >98% $Zr(acac)_4$) was used as a reactant to develop zirconia onto silica. The reactions and procedures of preparation have been previously discussed [25]. Variation in the amount of grafted zirconia was provided by reiteration of all the reaction cycles from 1 to 4. The amorphous nature and content of zirconia (2.6 wt.% and 8.4 wt% ZrO_2 for the 1st and 4th reaction cycles, respectively, Table 1) were determined employing X–ray diffraction [25]. In the present work we present results for the unmodified silica and for silica modified with 4 cycles of zirconia reaction. Specific surface area, $S_{BET,}$ for initial and modified oxides was measured in previous work using low temperature desorption of nitrogen [25], and values are given in Table 1. Additional measurements of S_{BET} were performed in the present work for PNCs. Polydimethylsiloxane (PDMS, Kremniypolymer, Zaporozhye, Ukraine, molecular weight $MW \approx 7960$, degree of polymerization d_p~105) was adsorbed onto dried oxide samples in the amounts of 40 and 80 wt.%. Different amounts of a hexane solution of PDMS at a constant concentration (1 wt.% PDMS) were added to fixed amount of dry silica–zirconia powder, up to the wanted polymer content. The suspension was mechanically stirred and finally dried at room temperature for 15–17 h and, subsequently, at 120 °C for 1.5 h [25]. Low PDMS content (40 wt.%) samples are powders similar to initial OX–50 powder, while at higher PDMS contents of 80 wt.% and 100 wt.% samples are liquid–like and liquid, respectively. Such materials are characterized by good hydrophilicity and porosity properties, which are easily controlled by surface grafting of hydrophobic polymers (PDMS here) and degree of particles aggregation [26,27], and are exploited for several biomedical and biochemical applications.

Five polymer nanocomposite compositions were prepared and studied in the present work, the initial PDMS, silica/PDMS with 40 and 80 wt.% PDMS and silica/zirconia/PDMS, containing modified silica with 4 cycles of zirconia, again with 40 and 80 wt.% PDMS. Based on previous work on similar systems [19], two PDMS loadings have been selected, 40 wt.% where interfacial effects dominate the behavior, and 80 wt.% where bulk behavior dominates, similarly to conventional NCs. Throughout the text and in the figures and tables, representative code names that describe the samples are used. For instance (i) *OX50Z4P40* corresponds to the sample in which PDMS at 40 wt.% is adsorbed onto OX–50 that had previously suffered 4 cycles of zirconia reaction (8.4 wt.% ZrO_2), and (ii) *OX50P80* corresponds to the sample in which PDMS at 80 wt.% is adsorbed onto OX–50 that has not suffered any zirconia reaction (unmodified).

2.2. Surface and porosity characterization

To analyze the textural characteristics of nanooxides (Table 1), low–temperature (77.4 K) nitrogen adsorption–desorption isotherms were recorded using a Sorptometer KELVIN 1042 (COSTECH Instruments) adsorption analyzer. Samples were previously outgassed at 473 K for several hours. The specific surface area (S_{BET}) was calculated according to the standard BET method [28] (details of calculations in Supplementary material SM.1).

2.3. Scanning electron microscopy (SEM)

Morphology was examined by field emission Scanning Electron Microscopy employing a FEI NovaSEM 230 apparatus at room temperature. SEM chamber operated at room temperature under high vacuum mode using a Helix detector at a voltage of 30 kV.

2.4. Differential scanning calorimetry (DSC)

Thermal properties of the materials were investigated in helium atmosphere in the temperature range from −170 to 20 °C using a TA Q200 series DSC instrument, calibrated with indium (for temperature and enthalpy) and sapphire (for heat capacity). Samples of ~8 mg in mass were closed in standard T–zero aluminum pans (for powders) or Tzero hermetic aluminum pans (for liquids). Samples were equilibrated in ambient conditions before measurements. Cooling and heating rates were constant at 10 K/min. PDMS crystals are melted at room temperature; therefore, a first heating scan to erase thermal history was not necessary here.

Table 1
Textural characteristics of initial oxides and oxide/PDMS composites: Specific surface area in total, $S_{BET,}$ of micropores, S_{micro}, mesopores, S_{meso}, macropores, S_{macro}, and respective specific pore volume, V_p, V_{micro}, V_{meso}, V_{macro}. R_V and R_S represent the average pore radii determined from the differential PSD with respect to pore volume and specific surface area, respectively.

Oxide	C_{ZrO2} (wt.%)	S_{BET} (m^2/g)	S_{nano} (m^2/g)	S_{meso} (m^2/g)	S_{macro} (m^2/g)	V_p (cm^3/g)	V_{nano} (cm^3/g)	V_{meso} (cm^3/g)	V_{macro} (cm^3/g)	$<R_V>$ (nm)	$<R_S>$ (nm)
OX50	0	58	5	52	1	0.096	0.002	0.081	0.013	13.3	4.3
OX50P40	0	18	0	17	1	0.023	0.0	0.016	0.007	23.5	4.3
OX50Z4	8.4	52	7	33	12	0.311	0.003	0.046	0.262	48.7	14.1
OX50Z4P40	8.4	18	0	17	1	0.022	0.0	0.015	0.007	26.8	4.5

2.5. Broadband dielectric spectroscopy (BDS)

Broadband dielectric spectroscopy (BDS) [29] measurements were carried out on samples of ~1 mm thickness for powders (compressed pellets) and ~50 μm thickness for liquids (employing thin silica spacers, to keep distance between the brass electrodes constant and ensure good electrical contacts). Samples were equilibrated under ambient conditions before measurements. The sample was inserted between brass plates forming an electrical capacitor. An alternate voltage was applied to the capacitor in a Novocontrol sample cell and the complex dielectric permittivity $\varepsilon^*=\varepsilon'-i\varepsilon''$ was recorded isothermally as a function of frequency in the broad range from 10^{-1}–10^6 Hz, at temperatures from −150 to 30 °C on heating (in nitrogen atmosphere) at steps of 2.5 K, 5 K and 10 K (depending on the process under investigation) using a Novocontrol Alpha analyzer. The temperature was controlled to better than 0.5 K with a Novocontrol Quatro cryosystem.

3. Results and discussion

3.1. Surface and porosity characterization (IPSD)

Nitrogen adsorption–desorption isotherms for neat oxides (OX50, OX50Z4) (Fig. 1, Table 1) [25] and after adsorption of PDMS at 40 wt.% (OX50P40, OX50Z4P40) demonstrate sigmoidal–shaped behavior with narrow hysteresis loops of the H3 type (Fig. 1a and c) [30,31]. This behavior indicates the formation of aggregates with initially non–porous particles that are characterized by textural porosity. With respect to IUPAC classification of pores, the nitrogen adsorption–desorption isotherms correspond to type II [30]. The distributions of voids between particles in aggregates (Fig. 1b) show that the textural characteristics of OX–50 change after modification. Although the values of the specific surface area S_{BET} (58 and 52 m^2/g for OX50 and OX50Z4, respectively, Table 1) do not show significant changes with nanozirconia modification, the gas adsorption modes changed (Table 1), suggesting certain differences in meso– and macroporosity. Furthermore, the shape of the adsorption–desorption isotherms of the NCs (Fig. 1c) and the analysis of the results suggest that nitrogen effectively fills mesopores in aggregates of initial OX–50 and mainly macropores of modified OX–50. We observe in Table 1 and Fig. 1b that the volume of mesopores (1 nm < R < 25 nm) of initial OX–50 (0.081 cm^3/g) decreases by a factor of about 2 after zirconia modification. Macroporosity (25 nm < R < 100 nm), on the contrary, increases by ~20 times for modified sample (OX50Z4). In general, the average pore radii (<R_V>, <R_S> in Table 1) are by 3–4 times larger in OX50Z4, as compared to unmodified OX–50.

The textural characteristics of the oxides were modified on adsorption of PDMS (Table 1 and Fig. 1d). The value of S_{BET} decreases by 69% and 65% (in comparison to the initial oxides) for OX50P40 and OX50Z4P40, respectively, after PDMS adsorption in the amount of 40 wt.% (Table 1). Polymer adsorption leads to suppression of pore volume (V_p) as well as of V_{meso} and V_{macro}. After addition of PDMS, the average pore radii (Table 1, <R_V> and <R_S>) decrease sharply. The adsorbed macromolecules can merge both the oxide nanoparticles and their aggregates into more compact structures, leading to decrease in the volume of voids between particles. This is a general effect in polymer/nanooxide composites [27].

3.2. Morphology (SEM)

Fig. 2 shows SEM images of the aggregates of OX–50 dispersed in OX50P80. One can clearly observe in Fig. 2a bunch–like structures varying between 250 nm and 1.5 μm in size. At higher magnification for the same sample in Fig. 2b the initial particles of OX–50 (~15–100 nm in diameter) structuring the larger aggregates can be recognized. Similar images were obtained for the zirconia modified nanocomposite samples. Micrographs of the developed zirconia nanoparticles onto the surfaces of silica have been shown in a previous study on initial oxides [25].

3.3. Thermal transitions (DSC)

3.3.1. Polymer crystallization

During cooling of OX–50/PDMS core–shell based NCs in DSC at 10 K/min from 20 °C to −170 °C single crystallization peaks were observed between −95 and −76 °C for all samples (Table 2, raw

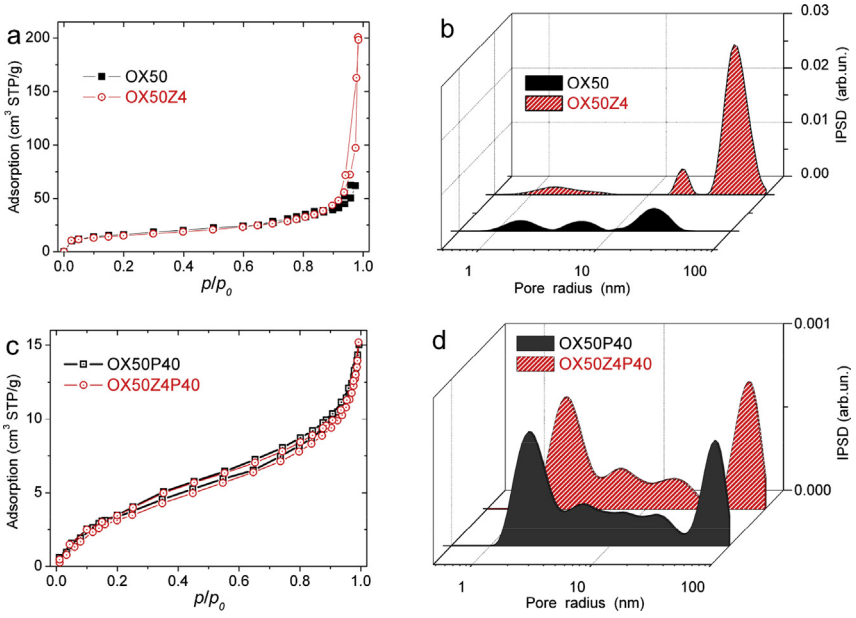

Fig. 1. Nitrogen adsorption–desorption isotherms (a,c) and incremental pore size distributions (b,d) of oxides before (a,b) and after adsorption of PDMS (c,d).

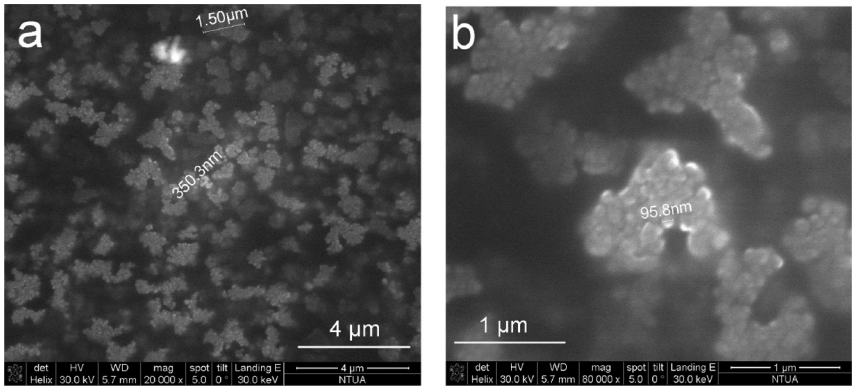

Fig. 2. SEM micrographs of OX50P80 composite.

Table 2
Quantities of interest from DSC measurements: crystallization temperature, T_c, degree of crystallinity, X_c, glass transition temperature, T_g, normalized heat capacity step at glass transition, $\Delta C_{p,n}$, interfacial and amorphous polymer fraction (at T_g), RAF_{DSC} and MAF_{DSC}, respectively, temperature maxima of melting peaks, $T_{m1,2}$.

Sample	T_c(°C) (±0.2)	X_c (wt) (±5%)	T_g (°C) (±0.5)	$\Delta c_{p,n}$ (J/gK) (±0.02)	RAF_{DSC} (wt) (±10%)	MAF_{DSC} (wt) (±10%)	T_{m1} (°C) (±0.2)	T_{m2} (°C) (±0.2)
OX50P40	−81	0.53	–	0.00	0.47	0.00	−48	−40
OX50Z4P40	−84	0.46	–	0.00	0.54	0.00	−48	−41
OX50P80	−80	0.57	−126	0.15	0.23	0.20	−48	−40
OX50Z4P80	−95	0.23	−129	0.04	0.68	0.09	−50	−39
PDMS	−76	0.65	−127	0.22	0.12	0.23	−47	−40

data in Supplementary material SM.2). During the subsequent heating in Fig. 3 the endothermic step of glass transition (−129 to −127 °C, Table 2) and cold crystallization exothermic peaks (−110 to −90 °C) are observed for neat PDMS and NCs with 80 wt.% PDMS. Finally, complex endothermic peaks during melting of PDMS were recorded for all samples between −55 and −35 °C (Table 2, measurement results in Supplementary material SM.2). The measured and calculated quantities of interest are shown in Table 2.

By normalizing the recorded crystallization enthalpy values, ΔH_c, to the same polymer content, X_{PDMS}, for each sample, the degree of crystallinity, X_c, was calculated according to Eq. (1)

$$X_c = \Delta H_c / (X_{PDMS} \cdot \Delta H_{100\%}) \quad (1)$$

where $\Delta H_{100\%}$ is the enthalpy of fusion of neat PDMS taken as 37.43 J/g [32].

Neat PDMS crystallizes at −76 °C and X_c is 0.65 wt (Table 2). Both crystallization temperature, T_c, and degree of crystallinity, X_c, are suppressed in all OX−50/PDMS samples. Suppression gets stronger with zirconia modification for both polymer loadings (Table 2). Crystallization during cooling at 10 K/min is very weak for OX50Z4P80 (Table 3), thus PDMS in this sample crystallizes partially during heating (cold crystallization [33], Fig. 3b). The results suggest that silica particles do not act as crystallization nuclei [33]). Results are similar to those presented here have been obtained in previous work on silica/PDMS NCs [32,34,35], as well as on polymers confined between solid surfaces [24].

At higher temperatures, complex endothermic melting peaks are observed between −50 and −39 °C (T_{m1}, T_{m2} in Table 2). The temperature difference between these two peaks varies between 7 and 11 K (Table 2). T_{m1} is lower in the case of NCs as compared to neat PDMS, suggesting lower density (worse lamellae packing [33,36]) of PDMS spherulites in OX−50/PDMS core−shell NCs. Complex and double melting peaks have been observed before in PDMS systems [10,19,32], probably related also with events of recrystallization and subsequent melting of metastable crystals [32,33,37]. Thus, X_c was not estimated from the melting enthalpy in the present work.

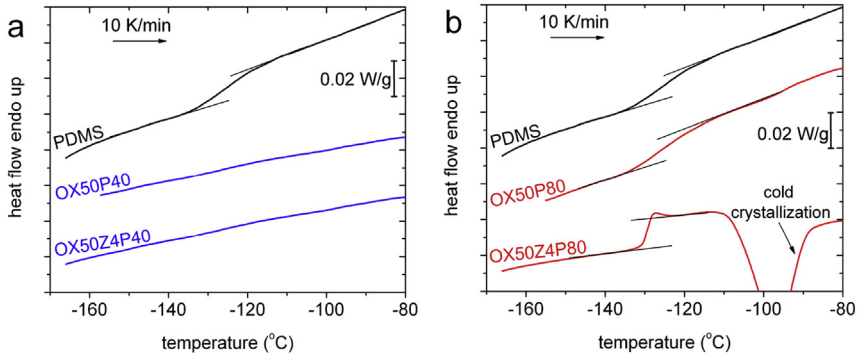

Fig. 3. Comparative DSC thermograms in the glass transition region of OX−50/PDMS, OX−50/Z4/PDMS and neat PDMS during heating at 10 K/min. (a) and (b) correspond to samples with 40 and 80 wt.% PDMS, respectively. The curves are normalized to sample mass. The lines represent the baselines of the thermograms before and after glass transition.

Table 3
Values of interest from BDS results: Shape parameters, α_{HN} and β_{HN}, and fragility index, m, for the recorded dielectric relaxations, interfacial polymer fraction, $X_{int,BDS}$, and mobile amorphous fraction, MAF_{BDS}, at ~ −95 °C. (*) corresponds to relaxations which do not obey VTFH equation.

Process parameter / Sample	α			α_c			α_{int}			$X_{int,BDS}$ (vt)	MAF_{BDS} (vt)
	α_{HN}	β_{HN}	m	α_{HN}	β_{HN}	m	α_{HN}	β_{HN}	m		
OX50P40	–	–	–	0.23	1.0	72	0.47	1.0	*	0.05	0.42
OX50Z4P40	–	–	–	0.29	1.0	96	0.40	1.0	35	0.10	0.44
OX50P80	–	–	–	0.31	1.0	88	0.49	1.0	*	0.01	0.42
OX50Z4P80	–	–	–	0.27	1.0	82	0.30	1.0	49	0.11	0.67
PDMS	0.35	0.9	106	0.30	1.0	96	–	–	–	0.00	0.25

3.3.2. Polymer glass transition

Coming now to glass transition (Fig. 3), the corresponding exothermic step was recorded during heating for the high polymer content samples (i.e. 80 wt.%) and initial PDMS (Fig. 3b). The glass transition step is absent (or extremely weak) for samples of 40 wt.% PDMS (Fig. 3a). The characteristic temperature T_g, determined as the midpoint of the heat capacity step at glass transition, is −127 °C in neat PDMS and varies in the NCs between −126 (OX50P80) and −129 °C (OX50Z4P80) (Table 2). T_g and the change in heat capacity, $\Delta C_{p,DSC}$, are ruled by spatial and physical constraints imposed by, both, the presence of oxide nanoparticles (strong interfacial interactions) and condensed polymer crystal regions [10,19]. Thus, T_g should increase in the NCs, as compared to neat PDMS, due to PDMS–silica interactions and decrease due to lowering of crystallinity X_c (Table 2). The results in Table 2, in particular the decrease of T_g in OX50Z4P80, suggest that changes in crystallinity dominate over the effects of PDMS–silica interactions.

In addition to T_g, the temperature range of glass transition, T_{onset}–T_{end}, is worth discussing. In previous works [10,37] we have demonstrated the close dependence of T_{onset}–T_{end} on the degree of crystallinity X_c of PDMS. Looking now at Fig. 3b, we suggest that the smooth shaped glass transition steps (large T_{onset}–T_{end}) for initial PDMS and OX50P80 with higher T_g values correspond to highly crystallized polymer. The sharp shaped glass transition (small T_{onset}–T_{end}) of OX50Z4P80 with lower T_g, on the other hand, corresponds to a sample of highly suppressed degree of crystallinity (Table 2).

We recall at this point that the physical adsorption of PDMS onto silica is accompanied by the formation of hydrogen bonds between surface hydroxyls and the O atoms of the PDMS backbone [20,40]. The intensity of FTIR spectra in the region of O–H vibrations decreases with polymer adsorption (Supplementary material SM.3), the decrease being stronger in the NCs of modified oxides. The decrease suggests that a significant amount of free surface hydroxyls [40] are disturbed by PDMS chains. The disturbance is stronger for the zirconia modified oxides, suggesting that the number of contact points between silica and polymer chains increases with zirconia. Further support for that will be provided in the following DSC and BDS results.

The above discussion suggests that the particles–polymer interactions should be responsible for the formation of a rigid amorphous polymer fraction [4] in the interfacial layer, similarly to previous works in PDMS [9,10,19]. We proceed now with calculation of the various polymer fractions from the glass transition data, in particular the heat capacity step, $\Delta Cp,DSC$. According to Schick and coworkers [36,41], a '3–phase model' can be applied for the quantitative estimation of the various polymer fractions from DSC results. The three polymer fractions in this model are the crystalline fraction, CF (~X_c), the rigid (immobile) amorphous, RAF_{DSC}, which does not contribute to the glass transition, and the mobile amorphous, MAF_{DSC}, which undergoes glass transition. In the case that $X_c = 0$, RAF_{DSC} represents the immobilized polymer at the particle–polymer interfaces (i.e. $RAF_{DSC} = RAF_{int,DSC}$), whereas for $X_c \neq 0$ RAF_{DSC} should also include the rigid amorphous polymer part immobilized within polymer crystals (i.e. $RAF_{DSC} = RAF_{int,DSC} + RAF_{cryst,DSC}$) [36,42]. It has been suggested that RAF_{cryst} does not relax during glass transition [36] or that its relaxation may occur at temperatures close to melting, T_m, i.e. significantly higher than T_g of the bulk [42].

Thus, in terms of $\Delta C_{p,n}$ recorded by DSC and normalized to the same amorphous polymer fraction (Table 2) according to Eq. (2), we may calculate MAF_{DSC} and RAF_{DSC} using Eqs. (3) and (4), respectively.

$$\Delta C_{p,n} = \frac{\Delta C_{p,DSC}}{(1 - X_c)X_{PDMS}} \tag{2}$$

$$MAF_{DSC} = \frac{\Delta C_{p,n}}{\Delta C^{PDMS}_{p,amorphous}}(1 - X_c) \tag{3}$$

$$RAF_{DSC} = 1 - CF - MAF_{DSC} = 1 - X_c - \frac{\Delta C_{p,n}}{\Delta C^{PDMS}_{p,amorphous}}(1 - X_c) \tag{4}$$

where X_{PDMS} is the mass fraction of the polymer, and $\Delta C^{PDMS}_{p,amorphous}$ is the heat capacity step of fully amorphous unaffected PDMS, found equal to 0.33 J/gK from fast cooling measurements (quenching, Supplementary material SM.4). According to the widely used ATHAS Database [43] and Ref. 2 therein, ΔC_p of amorphous PDMS (in general over the various types) is equal to 0.37 J/gK, quite similar to our result. Bearing in mind that molecular dynamics of a polymer is related to its structure (e.g. chain–end groups, crosslinking density etc.) [33], we will use our experimental value (0.33 J/gK) for further calculations related to glass transition. Please note that according to the above equations, both mass fractions refer to the whole polymer mass in the NCs. For referring to the whole nanocomposite mass, RAF_{DSC} and MAF_{DSC} should be multiplied with X_{PDMS}. According to work in NCs based on semicrystalline polymers, the $RAF_{cryst,DSC}$ to X_c and $RAF_{cryst,DSC}$ to $RAF_{int,DSC}$ ratios may not be constant [4,41]. Moreover, the interfacial polymer fraction can be temperature dependent according to BDS [19]. Thus, we will not attempt to calculate separately these fraction and we will consider results by Eqs. (3) and (4) as simplified approximations for MAF_{DSC} and RAF_{DSC} at temperatures close to T_g.

The calculated values are listed in Table 2. RAF_{DSC} varies between 0.47 and 0.54 wt for the samples of low polymer loading and between 0.23 and 0.68 wt for the samples of high polymer loading. For neat PDMS, the respective value is 0.12 wt and it corresponds to $RAF_{cryst,DSC}$, while CF is 0.65 wt. Considering that X_c is in general lower for the NCs with modified oxides for both polymer loadings while, at the same time, RAF_{DSC} is higher (changes are systematic for 80 wt.% PDMS), we conclude that the increase on RAF_{DSC} originates from an increase of $RAF_{int,DSC}$.

In agreement with the values of V_p in Table 1, the increase of $RAF_{int,DSC}$ reflects the increasing of accessible volume for polymer chains in the macro–pores. According to DSC results (and BDS later) the calculated V_p distributions (Table 1) seem to describe better the adsorption of PDMS chains in the voids of OX–50 aggregates, rather than S_{BET}. Finally, by comparing the DSC results between unmodified and modified OX–50, we can follow in Table 2 that with formation of nanozirconia (8.4 wt.%, Table 1) polymer adsorption is enhanced (RAF_{DSC} increases) at the expenses of bulk mobility and crystallization (the sum $MAF + X_c$ decreases in Table 2).

3.4. Segmental dynamics (BDS)

BDS results are comparatively presented in the form of frequency dependence of the imaginary part of dielectric permittivity (dielectric loss), ε'' (Fig. 4, isothermal plots) for selected temperatures. Results for the same initial PDMS sample have been presented also in a previous study of ours [19]. We focus on segmental dynamics, i.e. on the dielectric relaxations α, α_c and α_{int} [10,19] corresponding to the calorimetric glass transition in Fig. 3 a,b. The origin of these relaxations (see below) has been described in our previous works on PDMS systems [9,10,19].

3.4.1. Raw data and analysis

In Fig. 4 a,b α relaxation at around 10^5 Hz at −110 °C is associated with the glass transition of the bulk amorphous unaffected polymer fraction [10,19,37]. This relaxation corresponds to the lower temperature sharp–shaped glass transition step in DSC for the amorphous part of the polymer (Fig. 3b). Next to α, at around 10^3 Hz at −110 °C in Fig. 4 a,b, α_c relaxation originates from polymer chains restricted either between condensed crystal regions [10,38,39] (which is the case of neat and 80 wt.% PDMS, Fig. 4b) or in the voids between nanoparticles in their aggregates (which is the case of core–shell NCs at low polymer loading, Fig. 4a) [19]. Finally, α_{int} relaxation in the broad range from $5 \cdot 10^0$–10^2 Hz at −80 °C (Fig. 4 c,d) represents the dynamics of semi–bound polymer chains in the interfacial layer, with strongly reduced mobility due to interactions with the surface hydroxyls of OX–50 [9,19].

BDS results were analyzed by fitting model functions to the experimental data [44] in order to evaluate the time scale (temperature dependence of the frequency of maximum ε''), the dielectric strength (representative of populations of the relaxing molecular groups), and the shape parameters of the recorded relaxations. To that aim we employed the Havriliak–Negami (HN) equation [45].

$$\varepsilon^*(f) = \frac{\Delta\varepsilon}{(1 + (if/f_0)^{\alpha_{HN}})^{\beta_{HN}}} \quad (5)$$

A sum of up to three HN terms of the type (5), one for each of the three relaxations α, α_c, and α_{int}, was fitted to the experimental data at each temperature and the fitting parameters were determined. The number of terms needed was different for different compositions and temperatures, depending on the number of relaxations present and the extent of their overlapping. In Eq. (5), $\Delta\varepsilon$ is the dielectric strength, f_0 is a characteristic frequency related to the frequency of maximum loss (ε''), and α_{HN} and β_{HN} are the shape parameters of the relaxation. We recall that the deviation of β_{HN} from 1 describes the asymmetry of the relaxation, whereas the deviation of α_{HN} from 1 the broadening of the relaxation. Thus, the symmetric Debye relaxation with a single relaxation time is characterized by $\alpha_{HN} = 1$, $\beta_{HN} = 1$ [45].

Values of the fitting parameters for the shape of the relaxations (mean values over the temperature range of measurements) are listed in Table 3. By plotting the frequency of maximum of ε'' from Eq. (5) against reciprocal temperature for the three segmental relaxations, the Arrhenius plots of Fig. 5a were constructed. Included in the Arrhenius plots of Fig. 5a are the respective peak temperatures at the equivalent frequencies of DSC and TSDC [19] (i.e.

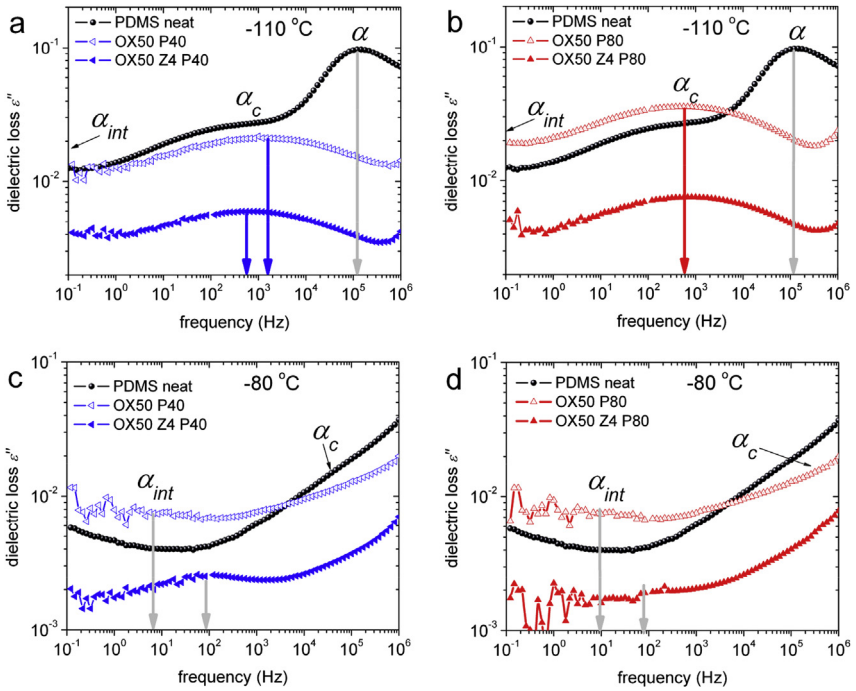

Fig. 4. Isothermal BDS plots of the imaginary part of dielectric permittivity (dielectric loss), ε'', vs frequency for PDMS and for composites with (a,c) 40 wt% adsorbed PDMS and (b,d) 80 wt.% PDMS, at −110 °C (a,b) and −80 °C (c,d). The arrows mark the frequency of ε'' maximum for each relaxation.

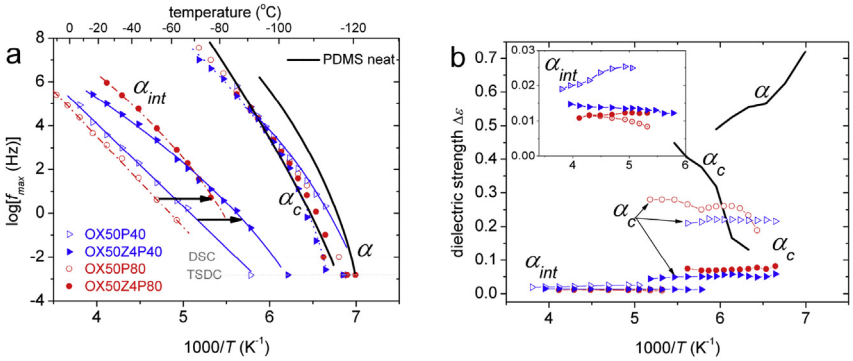

Fig. 5. (a) Arrhenius plots and (b) dielectric strength vs reciprocal temperature of the segmental relaxations: bulk polymer (α), restricted in voids and crystal regions (α_c) and interfacial polymer (α_{int}) for OX–50/Zr/PDMS composites and neat PDMS. The blue triangles correspond to 40 wt.% adsorbed PDMS, while the red cycles correspond to 80 wt.% adsorbed PDMS. Included in (a) are the respective DSC and TSDC points. The lines in (a) are fittings of the VTFH and Arrhenius equations [46] to the data for the recorded relaxations. The inset in (b) shows in more detail the region of α_{int} relaxation. The arrows in (a) mark changes on α_{int} between unmodified and modified OX–50. (For interpretation of the references to colour in this figure legend, the reader is referred to the web version of this article.)

20 mHz and 1.6 mHz, respectively [9]). TSDC (Thermally Stimulated Depolarization Currents) is a special dielectric technique in the temperature domain which was employed here to determine peak temperatures at the equivalent frequency of the technique. We refer to previous work on similar systems [19,34] for details of TSDC measurements. The Vogel–Tammann–Fulcher–Hesse (*VTFH*) equation (Eq. (7) in Ref. [10]), characteristic of cooperative processes [46] has been fitted to the data of Fig. 5a (lines) and the fragility index m was determined (Table 3). m is a measure of cooperativity (deviation from linear behavior) [19,46]. VTFH could not be fitted to the data for α_{int} in OX50P40 and OX50P80, which are described by the Arrhenius equation (Eq. (6) in Refs. [10], straight lines in Fig. 5a). Finally, we present in Fig. 5b the reciprocal temperature dependence of $\Delta\varepsilon$ from Eq. (5) for the relaxations of all measured samples.

3.4.2. Bulk dynamics (α and α_c relaxations)

We discuss separately bulk dynamics (α and α_c relaxations) in this section and interfacial dynamics (α_{int}) in the next section. The dual character of α_c relaxation (characterized by shape parameters α_{HN}~0.25, $\beta_{HN} = 1$, mean values over the temperature range of the relaxation), concerning the type of spatial restriction of PDMS chains (between PDMS crystals [10,38] and in voids of OX–50 aggregates), is better revealed by dividing the discussion into low (40 wt.%) and higher polymer contents (80–100 wt.%). For the low PDMS content, α_c originates from the reduced segmental mobility of PDMS chains inside the voids in the layers above the interfacial layer. In Fig. 4a and Fig. 5 a,b we follow that in theses samples time–scale and strength of α_c are suppressed with zirconia. This result is consistent with the simultaneous increase of the interfacial layer in the voids of OX–50 (Table 2), which increases the constraints imposed on polymer bulk–like mobility. Recalling DSC results, it is worth to point out the absence of glass transition for the 40 wt.% PDMS NCs (Fig. 3a). On the other hand, owing to the higher resolving power of BDS, both the interfacial (α_{int} in Fig. 4c) and the bulk–like segmental dynamics (α_c in Fig. 4a) are recorded by BDS in these NCs.

For the high polymer loading, α_c relaxation seems to dominate the segmental response of PDMS in Fig. 4b. In addition, the frequency–temperature position of α_c in Fig. 5a is almost identical for these samples, contrary to α_c for low polymer loading which slows down with nanozirconia modification. We recall that the DSC results for 80 wt.% PDMS samples and neat PDMS (Fig. 3 and supplementary material SM.2) show crystallization events (either at cooling or at heating, at 10 K/min). Considering that during BDS measurements the samples stay at each temperature of measurements for about 10 min (isothermals), this procedure of measurements could be considered as a type of multi–temperature crystallization annealing, which leads to increased degree of crystallinity, most probably higher than in DSC measurements. That is the reason for the same pattern of α_c relaxation in neat PDMS and the composites of 80 wt.% PDMS (Fig. 4b), despite different degrees of crystallinity by DSC (Table 2).

Bulk unaffected PDMS mobility is recorded via α relaxation only for the initial PDMS in Fig. 4a (α_{HN}~0.35, $\beta_{HN} = 0.9$, Table 3). The absence of unaffected polymer mobility (bulk) in the NCs reveals the high degree of constraints imposed on polymer mobility in these highly complex systems.

3.4.3. Interfacial dynamics (α_{int} relaxation)

The relaxation process of PDMS in the interfacial layer (α_{int}, characterized by mean values of the shape parameters over the temperature range of the relaxation α_{HN}~0.30–0.49, $\beta_{HN} = 1$) on the surfaces of OX–50 (inner walls in the voids and external walls of the aggregates) is the slowest of the three segmental relaxations. The assignment of this process to PDMS in the interfacial layer is supported by the following observations are: (i) α_{int} is absent in neat PDMS, (ii) its time–scale trace extrapolated to the respective DSC equivalent frequency (~10^{-2} Hz [9]) approaches the region of T_g, and (iii) its $f_{max}(T)$ dependence is, in general, of the VTFH type [10,19] revealing its cooperative character. Similar results have been obtained recently by employing BDS in NCs of various polymers [11,12,47].

For both polymer loadings in Fig. 5a α_{int} is slower for unmodified OX–50 than for zirconia modified samples. α_{int} immigrates towards higher frequencies/lower temperatures and its cooperativity increases (increased m, Table 3) with surface modification (zirconia content 8.4 wt.%, Table 1), suggesting enhancing of polymer dynamics at the OX–50/PDMS interface. At the same time, $\Delta\varepsilon$ for α_{int} in Fig. 5b exhibits higher values for the lower PDMS loading NCs. The same is true for dielectric permittivity (ε') and AC conductivity (σ_{AC}) (Supplementary material SM.5), which are, however, higher than additivity values [48]. These results can be rationalized in terms of increased orientational polarization in the interfacial layer, at the lower PDMS content (to be further discussed below), in agreement with results reported recently for similar systems [19].

The fraction of polymer in the interfacial layer (the reduced mobility polymer fraction) $X_{int,BDS}$ was calculated by the following equation [10],

$$X_{\mathrm{int},BDS} = \frac{\Delta\varepsilon_{a,\mathrm{int}}(1 - X_c)}{\Delta\varepsilon_{\alpha,\mathrm{int}} + \Delta\varepsilon_{\alpha+a_c}} \quad (6)$$

where $\Delta\varepsilon$ is the dielectric strength of each relaxation and X_c is the degree of crystallinity for each sample (obtained by DSC, Table 2). Bearing in mind that the dielectric strength changes with temperature, we employed BDS results at a temperature (−95 °C) where all relaxations were simultaneously recorded. The use of Eq. (6) implies the assumption of equal polarizability of PDMS chains independently of their location at the interface or in the bulk. Evidence against this assumption will be provided later in this section [49]. Nevertheless, we keep Eq. (6) as first approximation for calculating $X_{int,BDS}$ and comparing with RAF_{DSC}. Equation (6) is analog to Eq. (4) (used for DSC calculation of RAF_{DSC}), as both employ the whole polymer response and refer to the whole polymer amount. It should be pointed out that the contribution of interfacial polymer fraction is additive in BDS measurements (addition of α_{int} relaxation), whereas in DSC measurements RAF_{DSC} was estimated more indirectly, through the missing of the corresponding contribution to the heat capacity jump at the glass transition (reduction of $\Delta C_{p,n}$). Results of $X_{int,BDS}$ are listed in Table 3 and are shown in Fig. 6a comparatively with those of DSC.

Similar to RAF_{DSC} (Table 2), $X_{int,BDS}$ calculated by BDS increases with surface modification of OX–50. We recall that, in addition to $X_{int,BDS}$ increase (Fig. 6a), the dynamics at the interface is also accelerated (Fig. 5a). These effects on interfacial polymer fraction and dynamics are systematic (although weak) with the amount of surface modification in the samples containing silica modified with 1 and 4 cycles of zirconia reaction (data shown in supplementary material SM.6). We suggest that the increase of the concentration of contact points at the interfaces accessible to PDMS is at the origin of both these results (inset to Fig. 6a).

The insets to Fig. 6a show the simplified model employed for the interpretation of our results. According to this model and previous experimental findings obtained with silica/PDMS core–shell systems with high surface area fumed silica [19], it is suggested that adsorption of PDMS proceeds via two chain conformations, which can be considered responsible for the molecular mobility recorded by BDS as interfacial α_{int} relaxation process: (a) extended tails forming the outer region, with bulk–like density but reduced mobility and (b) flattened chain segments which form the inner quite dense region due to multiple contact points (loops) with the silica surface (insets to Fig. 6a) [22]. It has been also suggested that for low polymer contents the tails are mobile enough to cooperate with each other, but being sparsely distributed on the surfaces of the nanoparticles their cooperativity length (ξ) [46] is relatively large [19]. The extended (orientated) tails imply high polarizability and, this way, increase ε', ε'' and $\Delta\varepsilon$, in agreement with experimental results obtained with PDMS adsorbed on high surface area silica [19]. Similar results have been obtained here for the 40 wt.% PDMS systems. In addition, surface modification of OX–50 by zirconia in the present work leads to increased number of contact points and, therefore, more dense interfacial layer. This implies reduction of the cooperativity length ξ and, thus, in the frame of Adam–Gibbs theory [50], faster and more cooperative segmental dynamics, in agreement with results for α_{int} in the present work (Fig. 5a, Table 3). The additional polymer chains that connect to the additional contact points (in agreement to FTIR, discussion in section 3.3.2) can form both extra tails and loops. This implies serious obstacles to the orientation of the tails, resulting in reduction of dielectric response ($\Delta\varepsilon$ and ε', in Fig. 5b and Supplementary material SM.5, respectively).

So far the discussion was limited to the 40 wt.% PDMS NCs. $X_{int,BDS}$ for samples of 80 wt.% adsorbed PDMS are again in close qualitative agreement with DSC (Fig. 6a). Also, interfacial dynamics accelerates systematically with zirconia in Fig. 5a. In addition, *MAF* follows opposite trends with zirconia modification for DSC and BDS in Fig. 6b (and Supplementary material SM.6) for the high PDMS loading, while *MAF* for the low polymer loading is almost constant for both DSC and BDS. These results reflect, on the one hand, the suppression of interfacial polarizability at high polymer loading (ε' in Supplementary material SM.5) and, on the other hand, the significance of the degree of crystallinity in the determination of *MAF* ($MAF = 1 - X_c - RAF$). Kumar and coworkers pointed to the primary role of crystallization in semicrystalline PNCs, affecting also filler distribution and aggregation [51].

Increased orientational polarizability in the interfacial layer as compared to bulk is also at the origin of differences in the absolute values of $X_{int,BDS}$ and RAF_{DSC} and in their dependence on surface modification in Fig. 6a. It is interesting to note in this connection the significantly lower dielectric response of the NCs of the present study, as compared to similar NCs based on high surface area silica in a previous study [19]. Please note also that the two procedures of determining X_{int}, based on different experimental methods, are different in principle. So, as

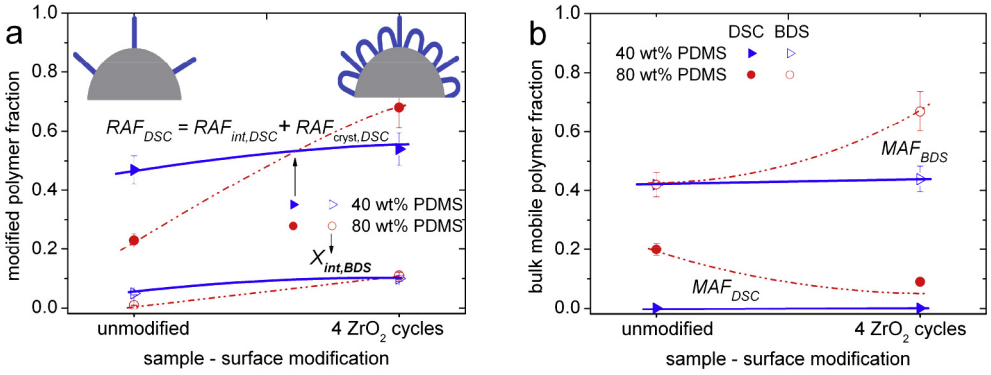

Fig. 6. Estimated (a) modified polymer fractions (RAF_{DSC}, $X_{int,BDS}$), and (b) bulk mobile amorphous polymer fraction, *MAF*, against surface modification of initial OX–50 particles with nanozirconia, for systems loaded with 40 wt.% PDMS (blue triangles) and 80 wt.% PDMS (red cycles). Results for RAF_{DSC} are shown comparatively at T_g (solid symbols) and for $X_{int,BDS}$ at −95 °C (empty symbols) (details in text). The lines are used as guides to the eyes. The insets to (a) show simplified models for the conformations of polymer chains during the first stages of adsorption on the surface of silica at 40 wt.% PDMS loading for the different surface modifications of OX–50. (For interpretation of the references to colour in this figure legend, the reader is referred to the web version of this article.)

mentioned previously, $X_{int,BDS}$ was determined through the contribution of interfacial polymer fraction to total polarization (Eq. (6)), while RAF_{DSC} (Eq. (4)) through the missing of the corresponding contribution to the heat capacity jump at the glass transition.

In Fig. 7 we compare time scale of interfacial dynamics in the present and in previous works in (a) conventional PDMS/silica and PDMS/titania NCs, i.e. spherical nanoparticles *in situ* generated and dispersed in a matrix of crosslinked PDMS [9,10], and (b) in core–shell systems based on high specific surface area silica and linear PDMS [19].

The traces of the recorded α_{int} in the present study (Fig. 7) are, in general, similar to those of conventional [10] and core–shell based [19] silica/PDMS from previous work. Differences for different types of filler, i.e. slower for conventional titania/PDMS than for silica/PDMS, grey dash–dotted lines (2) and (1), respectively, in Fig. 7 [10], have been previously ascribed to stronger hydrogen bonding between PDMS and the –OH of titania [20] as compared to silica [10,34]. Evidence against this interpretation was provided in a previous study of PDMS adsorbed on fumed silica and silica gel (with high S_{BET} for both) [19], where the traces of α_{int} in the Arrhenius plot at 40 wt.% and 80 wt.% polymer loadings were found to coincide with those of titania/PDMS and silica/PDMS [10], respectively. Moreover, thermal annealing of the systems at the temperature of PDMS crystallization was found to suppress significantly both dynamics and strength of α_{int} relaxation, especially in the case where PDMS crystallization was absent (i.e. for NCs with 40 wt% PDMS, red dotted lines (3) and (4) in Fig. 7 [19]).

Combining all the above observations we suggest that the strength of polymer–particle hydrogen bond is not the main factor dominating interfacial dynamics. Our results provide evidence that interfacial dynamics is mainly ruled by: (a) the number and accessibility of contact points (surface properties of the particles) and (b) structure and flexibility of polymer chain (polymer topology at the interfaces). The results of the present study could be explained by employing models proposed previously involving different conformations of polymers adsorbed onto a solid surface [22,23]. However, further work is needed to shed more light on these issues, such as by variation of type and size of the initial particles [19] along with changes in the interfacial hydration level [26,52].

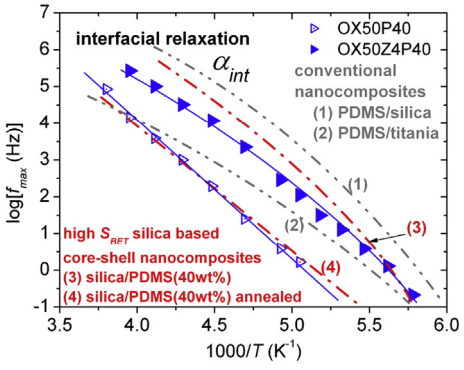

Fig. 7. Comparative Arrhenius plots of interfacial dynamics (α_{int}) in core–shell and conventional oxide/PDMS nanocomposites. Open and solid triangles correspond to OX50P40 and OX50Z4P40 core–shell systems, respectively (present work). Lines (1) and (2) correspond to the interfacial relaxation in conventional (sol–gel) PDMS/silica and PDMS/titania nanocomposites, respectively [10]. Line (3) corresponds to core–shell system based on fumed silica of high surface area (A380, S_{BET}~342 m^2/g) on which 40 wt% of PDMS has been adsorbed [19]. Line (4) corresponds to the interfacial relaxation of the same system after thermal (crystallization) annealing [19].

4. Conclusions

Structure, porosity and interfacial characteristics of low specific surface area (S_{BET}~58 m^2/g) fumed silica nanoparticles (~15–100 nm in average diameter), partly modified via nanozirconia grafting, along with polymer organization during polymer adsorption and preparation of core–shell based nanocomposites (NCs), were in the center of interest for this study. To that aim adsorption–desorption nitrogen isotherms, morphology (SEM), thermal (DSC) and dielectric (BDS) techniques were employed. From the fundamental point of view, this work provides additional evidence that the *core–shell* type NCs present an alternative model system for the investigation of interfacial dynamics: by controlling polymer content, the recorded DSC and BDS responses may be dominated by the interfacial polymer layer, being the majority among other polymer fractions.

Amorphous silica nanoparticles were found to aggregate with each other in the 10^2 nm scale, forming interparticle voids of the meso (1 nm < R_{void} < 25 nm) and macro (R_{void} > 25 nm) scale. Nanozirconia modification increased the macroporosity and simultaneously suppressed the mesoporosity in the aggregates. Results indicate that during the initial stages of polymer adsorption strong hydrogen bonding develops between the surface hydroxyls of silica and the oxygens on PDMS backbone, resulting in high coverage of both the inner and external surfaces of silica aggregates. Results by DSC and BDS, in agreement with each other, reveal higher degree of initial PDMS adsorption in the case of modified surfaces. This last result was obtained by monitoring the fraction and dynamics of polymer chains at the interface (α_{int} process), and interpreted in terms of increased density of contact points of silica (accessible hydroxyl groups) with PDMS chains. The increase of concentration of polymer chains at the interface is accompanied by faster dynamics and increased cooperativity. According to a previously proposed model [19], we suggest that during the initial adsorption of PDMS the chains are strongly attached (although sparsely distributed) and highly orientated (tails) over the surfaces, characterized by lower cooperativity. Nanozirconia modification increases the concentration of accessible to PDMS contact points and, thus, the number of tails. Further polymer adsorption proceeds via loop–like conformations, probably in more dense packing onto the surfaces, resulting in increase of the degree of cooperativity of polymer chains in the interfacial layer and in faster interfacial dynamics [19]. Thus, number and accessibility of contact points (surface properties of the particles) and structure and flexibility of polymer chain (polymer topology at the interfaces) dominate interfacial interactions. Further work along the lines of the present investigation by varying type and size of filler [19], surface modification and annealing procedure, partly in progress, is expected to provide further insight into polymer structure and dynamics in close proximity to solid surfaces.

Acknowledgments

This research has been co–financed by the European Union (European Social Fund – ESF) and Greek national funds through the Operational Program "Education and Lifelong Learning" of the National Strategic Reference Framework (NSRF) – Research Funding Program: Heracleitus II. Investing in knowledge society through the European Social Fund (P.K. and P.P.) and Research Funding Program: Aristeia (A.K. and P.P.). This research was partially supported by FP7 – PIRSES–GA–2013–612484 NANOBIOMAT. I.S. acknowledges support by the Visegrad Fund (Contract number 51300077).

Appendix A. Supplementary data

Supplementary data related to this article can be found at http://dx.doi.org/10.1016/j.polymer.2015.05.017.

References

[1] Paul DR, Robenson LM. Polymer 2008;49:3187–204.
[2] Jancar J, Douglas JF, Starr FW, Kumar SK, Cassagnau P, Lesser AJ, et al. Polymer 2010;51:3321–43.
[3] Schmidt DF, Giannelis EP. Chem Mater 2010;22:167–74.
[4] Wurm A, Ismail M, Kretzschmar B, Pospiech D, Schick C. Macromolecules 2010;43:1480–7.
[5] Akcora P, Liu H, Kumar SK, Moll J, Ki Y, Benicewicz BC, et al. Nat Mater 2009;8:354–9.
[6] Harton SE, Kumar SK, Yang H, Koga T, Hicks K, Lee HK, et al. Macromolecules 2010;43:3415–21.
[7] Rissanou AN, Harmandaris V. Soft Matter 2014;10:2876–88.
[8] Vogiatzis GG, Theodorou DN. Macromolecules 2014;47:387–404.
[9] Fragiadakis D, Pissis P. J Non–Cryst Solids 2007;353:4344–52.
[10] Klonos P, Panagopoulou A, Bokobza L, Kyritsis A, Peoglos V, Pissis P. Polymer 2010;51:5490–9.
[11] Füllbrandt M, Purohit PJ, Schönhals A. Macromolecules 2013;46:4626–32.
[12] Holt AP, Griffin PJ, Bocharova V, Agapov AL, Imel AE, Dadmun MD, et al. Macromolecules 2014;47:1837–43.
[13] Galaburda MV, Klonos P, Gun'ko VM, Bogatyrov VM, Borysenko MV, Pissis P. Appl Surf Sci 2014;305:67–76.
[14] Liu YL, Chen E. Coord Chem Rev 2010;254:1011–37.
[15] Klonos P, Pissis P, Gun'ko VM, Kyritsis A, Guzenko NV, Pakhlov EM, et al. Colloid Surf A: Physicochem Eng Asp 2010;360:220–31.
[16] Wang Y, Gao S, Ye W, Yoon HS, Yang Y. Nat Mater 2006;5:791–6.
[17] Rodriguez R, Herrera R, Bourlinos AB, Li R, Amassian A, Archer LA, et al. Appl Organometal Chem 2010;24:581–9.
[18] Nan A, Turcu R, Liebscher J. J Polym Sci A Polym Chem 2012;50:1485–90.
[19] Klonos P, Sulym IY, Borysenko MV, Gun'ko VM, Kripotou S, Kyritsis A, et al. Polymer 2015;58:9–21.
[20] Bokobza L, Diop AL. Express Polym Lett 2010;4:355–63.
[21] Gong S, Chen Q, Moll JF, Kumar SK, Colby RH. ACS Macro Lett 2014;3:773–7.
[22] Gin P, Jiang N, Liang C, Taniguchi T, Akgun B, Satija SK, et al. Phys Rev Lett 2012;109:265501.
[23] Rotella C, Napolitano S, Vandendriessche S, Valev VK, Verbiest T, Larkowska M, et al. Langmuir 2011;27:13533.
[24] Vanroy B, Wübbenhorst W, Napolitano S. ACS Macro Lett 2013;2:168–72.
[25] Sulim IY, Borysenko MV, Korduban OM, Gun'ko VM. Appl Surf Sci 2009;255:7818–24.
[26] Gun'ko VM, Turov VV, Bogatyrev VM, Zarko VI, Leboda R, Goncharuk EV, et al. Adv Colloid Interface Sci 2005;118:125–72.
[27] Gun'ko VM, Turov VV. Nuclear magnetic resonance studies of interfacial phenomena. Boca Raton: CRC Press; 2013.
[28] Brunauer S, Emmett PH, Teller E. J Am Chem Soc 1938;60:309–19.
[29] Kremer F, Schoenhals A, editors. Broadband dielectric spectroscopy. Berlin: Springer; 2002.
[30] Gregg SJ, Sing KSW. Adsorption, surface area and porosity. 2nd ed. London; New York: Academic Press; 1982.
[31] Kruk M, Jaroniec M. Chem Mater 2001;13:3169–83.
[32] Aranguren M. Polymer 1998;39:4897–903.
[33] Gedde UW. Polymer physics. London: Chapman & Hall; 1995.
[34] Klonos P, Panagopoulou A, Kyritsis A, Bokobza L, Pissis P. J Non–Cryst Solids 2011;357:610–4.
[35] Sulym I, Klonos P, Borysenko M, Pissis P, Gun'ko VM. J Appl Polym Sci 2014;131:41154. http://dx.doi.org/10.1002/app.41154.
[36] Dobbertin J, Hensel A, Schick C. J Therm Anal Calorim 1996;47:1027–40.
[37] Klonos P, Pandis Ch, Kripotou S, Kyritsis A, Pissis P. IEEE Trans Diel Electr Insul 2012;19:1283–90.
[38] Yu L, Cebe P. J Polym Sci Part B: Polym Phys 2009;47:2520–32.
[39] Papageorgiou GZ, Terzopoulou Z, Bikiaris D, Triantafyllidis KS, Diamanti E, Gournis D, et al. Thermochim Acta 2014;597:48–57.
[40] Gun'ko VM, Turov VV, Ruban AN, Kazanets AI, Leboda R, Skubiszewska–Zięba J. J Colloid Interf Sci 2013;394:467–74.
[41] Purohit PJ, Wang D, Wurm A, Schick C, Schönhals A. Eur Polym J 2014;55:48–56.
[42] Xu H, Cebe P. Macromolecules 2004;37:2797–806.
[43] Wunderlich B. Prog Polym Sci 2003;28:383–450.
[44] Data analysis software by Dr. Daniel Fragiadakis, http://grafitylabs.com/.
[45] Havriliak S, Negami S. Polymer 1967;8:161–210.
[46] Richert R, Angell CA. J Chem Phys 1998;108:9016–26.
[47] Fragiadakis D, Bokobza L, Pissis P. Polymer 2011;52:3175–82.
[48] Fragiadakis D, Logakis E, Pissis P, Kramarenko VY, Shantalii TA, Karpova IL, et al. J Phys Conf Ser 2005;10:139–42.
[49] Capponi S, Napolitano S, Wübbenhorst M. Nat Commun 2012;3:1233.
[50] Adam G, Gibbs JH. J Chem Phys 1965;43:139–46.
[51] Khan J, Harton SE, Akcora P, Benicewicz BC, Kumar SK. Macromolecules 2009;42:5741–4.
[52] Gee R, Maxwell RS, Balazs B. Polymer 2004;45:3885–91.